

# Dust Environment Modelling of Comet 67P/Churyumov-Gerasimenko

Jessica Agarwal, Michael Müller, and Eberhard Grün

**Abstract** Dust is an important constituent in cometary comae; its analysis is one of the major objectives of ESA's Rosetta mission to comet 67P/Churyumov-Gerasimenko (C-G). Several instruments aboard Rosetta are dedicated to studying various aspects of dust in the cometary coma, all of which require a certain level of exposure to dust to achieve their goals. At the same time, impacts of dust particles can constitute a hazard to the spacecraft. To conciliate the demands of dust collection instruments and spacecraft safety, it is desirable to assess the dust environment in the coma even before the arrival of Rosetta. We describe the present status of modelling the dust coma of 67P/C-G and predict the speed and flux of dust in the coma, the dust fluence on a spacecraft along sample trajectories, and the radiation environment in the coma. The model will need to be refined when more details of the coma are revealed by observations. An overview of astronomical observations of 67P/C-G is given and model parameters are derived from these data where possible. For quantities not yet measured for 67P/C-G, we use values obtained for other comets. One of the most important and most controversial parameters is the dust mass distribution. We summarise the mass distribution functions derived from the in-situ measurements at comet 1P/Halley in 1986. For 67P/C-G, constraining the mass distribution is currently only possible by the analysis of astronomical images. We find that the results from

---

Jessica Agarwal

ESA Research and Scientific Support Department, ESTEC, Postbus 299, NL-2200 AG Noordwijk, e-mail: [jagarwal@rssd.esa.int](mailto:jagarwal@rssd.esa.int)

Michael Müller

ESA, ESOC, Robert-Bosch-Str. 5, D-64293 Darmstadt, e-mail: [michael.mueller@esa.int](mailto:michael.mueller@esa.int)

Eberhard Grün

Max-Planck-Institut für Kernphysik, Saupfercheckweg 1, D-69117 Heidelberg, e-mail: [eberhard.gruen@mpi-hd.mpg.de](mailto:eberhard.gruen@mpi-hd.mpg.de)

such analyses are at present rather heterogeneous, and we identify a need to find a model that is reconcilable with all available observations.

## 1 Introduction

The inner comae of comets are the most dust rich environments in the solar system. Almost everything we see from a comet with the naked eye is dust. Both the coma and the tail are seen as sunlight scattered by  $\mu\text{m}$ -sized dust. Meteors, especially in meteor streams, are caused by mm- to cm-sized particles that originate to a large extent in comets. Fireballs are due to multi-ton boulders some of which are believed to stem from comets as well.

Spacecraft missions to comets must take careful precautions to survive the hazards of the cometary dust cloud. Special dust shields have been designed to protect the spacecraft. Nevertheless, the dust environment can have detrimental effects on some aspects of the missions. The Giotto spacecraft flew by comet 1P/Halley at a distance of 600 km and a speed of 70 km/s. During this close fly-by Giotto was hit by mm-sized dust particles. The impacts caused nutation of the spacecraft spin, and the data transmission was disrupted. Some experiment sensors suffered damage during this fly-by. Similarly, the 350-kg impactor of the Deep Impact probe experienced attitude disturbances from dust grains before it hit the nucleus of comet 9P/Tempel 1. Owing to the low velocity of Rosetta relative to the comet, the consequences of dust impacts will be much less severe than for the fly-by missions. But detailed knowledge of the dust environment will be vital for the planning of spacecraft operations at the comet and is thus of crucial importance to optimise Rosetta's scientific return.

One of the problems in characterising the dust environment of a comet is that information on the nucleus, its dust and gas release is very limited. Before 1986, observations of cometary dust was the domain of astronomers. The method of Finson and Probst [1] was the first to be used to determine the size distribution of dust from observations of the tail at visible wavelengths. High resolution astronomical images of cometary comae revealed jets and other structures in the inner parts, some of which formed spirals which rotated like water from a lawn sprinkler indicating discrete dust emissions from localised active parts of the nucleus. A consequence of observing in visible light is that the results are biased to particle sizes in the range of 1 to 10  $\mu\text{m}$ , because much smaller and much larger particles do not contribute significantly to the scattered light [2]. With the extension of the observable spectral range to infrared wavelengths, also the thermal emission of dust became accessible to astronomers. It revealed information on the abundance of larger grains and on the mineralogical composition of the dust, the latter from characteristic spectral features in the near and mid-infrared range.

Breakthroughs in understanding cometary constituents came with the space missions to several comets: Giotto and two VeGa spacecraft to comet 1P/Halley in 1986, Deep Space 1 to comet 19P/Borelly in 1999, Stardust to comet 81P/Wild 2 in 2004, and Deep Impact to comet 9P/Tempel 1 in 2005. Water and CO were identified as the main species in the gas, and dust particles made of carbonaceous and silicate materials ranging from nanometre to millimetre sizes were detected. Active areas and corresponding dust jets were identified in spatially resolved images of some of the comets visited by spacecraft [3, 4, 5, 6]. For 67P/C-G, however, such detail will only be observed when in 2014 the Rosetta spacecraft reaches the comet. Until then any information on the dust environment has to be derived from astronomical observations of the target comet or by assuming correspondence to other, better studied comets.

The purpose of the present paper is twofold: on the one hand, to give an overview of the current knowledge of the dust environment of comet 67P/C-G, and on the other hand, to provide estimates of such quantities as the spatial density, flux, and speed of dust in the coma as functions of location and time. These values are meant to support the planning of measurements of the instruments on board Rosetta. Section 2 contains an overview of the available astronomical observations of comet 67P/C-G, and measurements of the albedo and temperature of dust from 67P/C-G are presented. In addition, the phase function, size distribution and radiation pressure efficiency of cometary dust are defined and discussed. In Section 3, several methods are presented to derive dust properties from modelling of images of the cometary tail or trail, and results for 67P/C-G that were obtained by several authors are discussed. Finally, in Section 4, the ESA Cometary Dust Environment Model [7, 8, 9, 10] is briefly described and results from applying it to comet 67P/C-G are presented.

## 2 Observations of 67P/C-G Dust and Dust Properties

In this section, we give an overview of the available observational data containing information on the dust of 67P/C-G, and we introduce and discuss the major quantities that can be measured by means of such observations. Some of these quantities (the dust size distribution, the radiation pressure efficiency and the emission speeds) can – in the absence of in situ measurements – only be inferred through modelling of astronomical images, which is discussed in Section 3. Published astronomical data on the dust of 67P/C-G include images of the dust coma, tail and trail in both visible and infrared light. They are available from 1982 onwards.

## 2.1 *Disambiguation: Dust tail, antitail, neckline, and trail*

In the following we give the definitions of some observational dust phenomena associated with comets as they are used in this paper:

Outside the inner coma – in which the dust is accelerated by gas drag – dust dynamics is dominated by solar gravity and radiation pressure. Both forces follow a  $1/r_h^2$ -law ( $r_h$  being the heliocentric distance) but act in opposite directions. Consequently, their ratio  $\beta$  depends only on the material properties of the dust grains, such as size, composition, density, and shape. In general, radiation pressure is most efficient for particles of about the size of the dominant wavelength of the radiation. Such grains are driven away from the nucleus in the direction opposed to the Sun and trailing the nucleus, thus forming the comet’s *dust tail* before they disperse into interplanetary space.

The term *antitail* refers to a part of the tail that seems to point toward the Sun instead of away from it. Often, this is a projection effect that occurs when the observer is in such a position that part of the normal tail appears to be on the Sun-facing side of the nucleus. Viewed in three dimensions, there is no difference between an ordinary tail and a projection antitail, but the dust seen in the antitail tends to be the larger and older component of the dust in the tail.

A *neckline* [11, 12, 13] consists of large particles emitted at a true anomaly of  $180^\circ$  before the observation: The orbital periods of large particles are similar to that of the parent comet. Their orbits are generally inclined with respect to the comet orbit, but the particles cross the orbital plane of the comet twice during each revolution around the Sun. One intersection point is the point of emission. The other lies on the line of nodes connecting the emission point and the Sun. The position of the second intersection point on the line of nodes depends on the emission velocity and  $\beta$  of the particle. Large particles emitted at a given time cross the orbital plane of the comet almost simultaneously, but at different positions along the nodal line. To an observer in – or close to – the comet orbital plane, they appear as a bright line, the neckline. Necklines can appear both in the Sun- and the anti-Sun direction i.e. can contribute to the tail as well as to the antitail. In the case of comet C1995 O1 Hale-Bopp in early 1997 the neckline was mainly visible along the tail direction, but also gave rise to an antitail [14].

The *dust trail* of a comet consists of mm- to cm-sized particles that – because of low emission speeds and little sensitivity to radiation pressure – remain close to the comet orbit for many revolutions around the Sun and whose appearance reminds of an airplane contrail. Trails of eight short-period comets were first observed with IRAS in 1983 [15, 16, 17], one of them being that of 67P/C-G.

## 2.2 Morphology of Coma, Tail, Antitail and Trail

The coma of 67P/C–G showed azimuthal brightness variations during both the 1996/97 and the 2002/03 apparitions [18, 19, 20, 21]. An example is displayed in Figure 1. The bright regions have been interpreted as border lines of coma fans produced by active areas at different latitudes on the rotating nucleus. The 2003 fan pattern suggests the presence of 2 or 3 active regions on the nucleus. For the 2-active-region scenario, the rotation axis requires to be very much inclined to the orbital plane, while for the 3-active-region scenario a very wide range of rotation axis directions is possible (H. Bönhardt, private communication). The azimuthal direction of the bright features has been used to constrain the orientation of the rotation axis of the nucleus [21, 18].

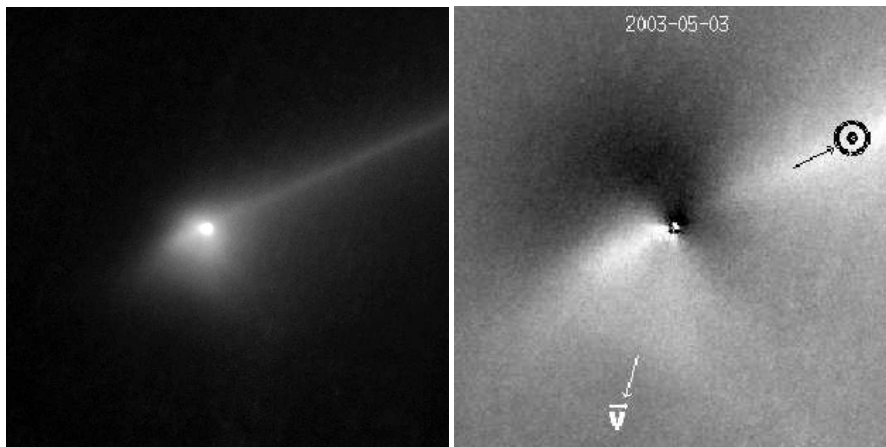


**Fig. 1** Left: Broadband R image of comet 67P/C–G on 3 May 2003 obtained with FORS1 at ESO/VLT/U1 [19, 20]. Right: Same image, but structurally enhanced by subtracting the azimuthally averaged coma profile from the measured brightness distribution. Distinct features in the coma are clearly visible. The image is a reproduction of Figure 1 (lower left) in [20], courtesy by R. Schulz.

The tail of 67P/C–G was characterised by a thin, bright feature close to the projected comet orbit and pointing away from the nucleus in the direction opposed to the motion of the comet. This feature was first observed shortly after perihelion in August 2002 and prevailed at least until April 2006 when the comet had already passed aphelion [22, 23, 24, 25, 26]. Different interpretations of this phenomenon are discussed in Section 3 with the conclusion that it most probably was a very pronounced antitail due to the low inclination of the comet orbit with respect to the ecliptic.

The dust trail of 67P/C–G was first observed with the Infrared Astronomical Satellite (IRAS) in 1983 [15, 16, 17] with a reported length of  $1.2^\circ$  in mean anomaly and a width of 50000 km. In visible light, observations of the

67P/C–G trail were done in 2002/03 at heliocentric distances between 1.3 AU and 3.1 AU [26] and in 2004 at  $r_h = 4.7$  AU (out-bound) [24]. Infrared observations of the 67P/C–G trail between 2004 and 2006 were obtained with the MIPS instrument of NASA’s Spitzer Space Telescope at  $24\mu\text{m}$  [27, 25].

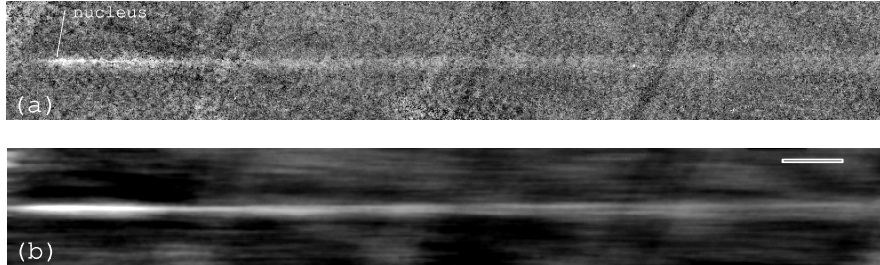


**Fig. 2** Reproduction of Figure 1 in [24]. The images show the dust trail and neckline of 67P/C–G in April 2004. The data were obtained with the Wide Field Imager (WFI) at the ESO/MPG 2.2m telescope in La Silla with a total exposure time of 7.5 hours and without filter. The size of the images is  $35' \times 4.7'$  each, corresponding to  $1.1^\circ$  in mean anomaly parallel to the orbit. (a) Unfiltered image. (b) Same image, each pixel being replaced by the average over a neighbourhood of 200 pixels ( $140''$ ) parallel and 10 pixels ( $7''$ ) perpendicular to the trail axis after removal of the nucleus. The filtering window is indicated in the upper right corner of (b). A detailed discussion of the data acquisition, processing and interpretation is given in [24] and modelling results are given in Section 3.3.

### 2.3 Albedo and Phase Function

The geometric albedo  $p$  of an object is defined as the ratio of the intensities reflected backwards by the object and by a totally diffusely reflecting (i. e. Lambert scattering) disc of the same geometric cross section [28], while the Bond albedo  $A_B$  is the ratio of the total light reflected from a sphere to total light incident on it [29]. The phase angle  $\alpha$  is the angle between the directions of the observer and of the incident radiation as seen from the scattering particle. The phase function  $j(\alpha)$  describes the ratio of intensity scattered in the  $\alpha$ -direction to the intensity scattered at  $\alpha = 0$ , and the integral of the phase function over  $4\pi$  solid angle is called the *phase integral*,  $q$ . The Bond and geometric albedos are related by  $A_B = qp$ .

To derive the dust phase function from astronomical observations, an object must be observed at different phase angles, i. e. at different times. Since the total cross section of dust is not constant with time, an appropriate normalisation is required, for which two methods are used. One method employs gas production rates measured simultaneously with  $Af\rho$  for normalisation [30, 31, 32], assuming that the dust-to-gas ratio as well as the dust size

distribution and material properties remain constant over time. The other method, preferable but more laborious, normalises the scattered intensity to the simultaneously measured thermal infrared emission from the same volume [33, 34, 35, 36, 37, 38, 39]. The general shape of the phase function of cometary dust is characterised by a distinct forward and a gentle backscattering peak and is rather flat at medium phase angles [40]. Divine [41] derived from data given in [37, 38, 39] the phase function shown in Figure 3 (solid line). The figure also shows the geometric phase function that describes the phase angle dependence of  $Af\rho$  and is discussed in Section 2.4.

Laboratory measurements and theoretical studies suggest that the dust albedo depends on particle size [42]. Earth based observations have so far not been suitable to investigate this dependence, because coma observations only provide data for the ensemble of particles of all sizes along a line of sight.

The geometric albedo is derived from the simultaneous observation of the scattered visible and the thermally emitted infrared light, either directly at  $\alpha = 0$ , or at multiple phase angles and assuming a given phase function. The geometric albedo of dust in the coma of 67P/C-G derived from the optical and infrared brightness was 0.04 at  $1.25\ \mu\text{m}$  and 0.05 at  $2.2\ \mu\text{m}$  [34], which is in accordance with a large sample of comets [43, 35]. From the low albedo it is inferred that there is no significant population of cold, bright (and possibly icy) grains that would contribute to the scattered light but not to the thermal emission [34]. There is, however, some indication that the geometric albedo is higher for comets beyond 3 AU [35], which may point in the same direction.

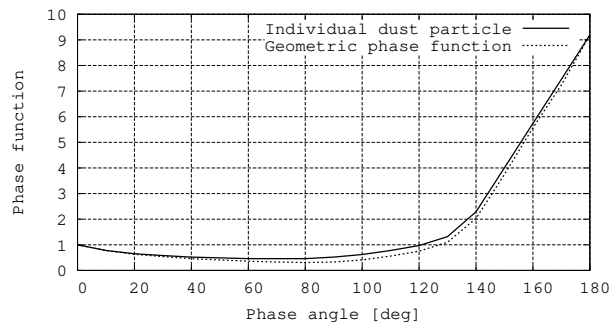


**Fig. 3** Solid line: phase function of an individual dust particle as given in [41], but here normalised to  $j(\alpha = 0) = 1$ . Dashed line: geometric phase function  $j_{\text{geo}}(\alpha)$  [9] accounting for the anisotropy of an axis-symmetric coma with peak activity at the subsolar point.

## 2.4 *Afρ* and Gas Production

The brightness of a cometary coma is proportional to the dust production rate. To infer the production rate from data obtained under different observational circumstances, the measured brightness must be corrected for all other parameters on which it depends. The quantity  $Af\rho$  was defined for this purpose [44].  $Af\rho$  stands for the product of albedo  $A = pj(\alpha)$  (see Section 2.3), filling factor  $f$  of grains within the field of view, and the radius  $\rho$  of the aperture at the comet. It is measured as follows:

$$Af\rho = 4 \frac{\Delta^2 (r_h/1\text{AU})^2}{I_{\text{sun}}^{(\text{filter})}} \times \frac{I_{\text{dust}}^{(\text{filter})}}{\rho}, \quad (1)$$

where  $r_h$  and  $\Delta$  are the heliocentric and geocentric distances of the comet during the observation, and  $\rho$  is the radius of the circular aperture on which the coma intensity  $I_{\text{dust}}^{(\text{filter})}$  was measured using a given filter.  $I_{\text{sun}}^{(\text{filter})}$  is the intensity of the Sun at 1 AU heliocentric distance seen through the same filter. Provided that the dust particles move away from the nucleus on straight trajectories and are not subject to processes altering their scattering behaviour,  $Af\rho$  is independent of the employed aperture radius, of the heliocentric and geocentric distances, and – to the extent that the dust can be considered as “grey” – of the spectral band in which the observation was carried out.

For an isotropic coma and discrete dust sizes  $s_j$ ,  $Af\rho$  is related to the production rates  $Q_{d,j}(s_j)$  via the dust emission speeds  $v_{d,j}$ , the geometric albedo  $p$ , and the phase function  $j(\alpha)$  [9]:

$$Af\rho = 2\pi p j(\alpha) \sum_j s_j^2 \frac{Q_{d,j}}{v_{d,j}}. \quad (2)$$

The relative magnitudes of the  $Q_{d,j}$  rates are given by the size distribution.

$Af\rho$  depends on the phase angle of the observation, due both to the scattering properties of a single dust grain [32] and – unless the coma is isotropic – to projection effects [9]. In a non-isotropic coma, the timescale on which the particles leave a given field of view depends on the angle between the main emission direction and the line of sight, with higher measured  $Af\rho$  for a line of sight parallel or close to the main emission direction. The phase-angle dependence of  $Af\rho$  is then better described by a *geometric* phase function  $j_{\text{geo}}(\alpha)$  [9] than by that of a single particle. The geometric phase function is characteristic of the specific pattern of emission of a given nucleus.

In practice,  $Af\rho$  often depends on the aperture size despite its definition [32, 18, and references therein]. This implies that the brightness distribution in the coma deviates from the assumed  $1/\rho$ -profile. Possible causes for this deviation include changes in the physical properties of the grains as they travel outward (e. g. loss of volatiles or fragmentation), the action of radiation



pressure modifying the straight trajectories of small particles inside the field of view, or a long-lasting population of large particles [32].

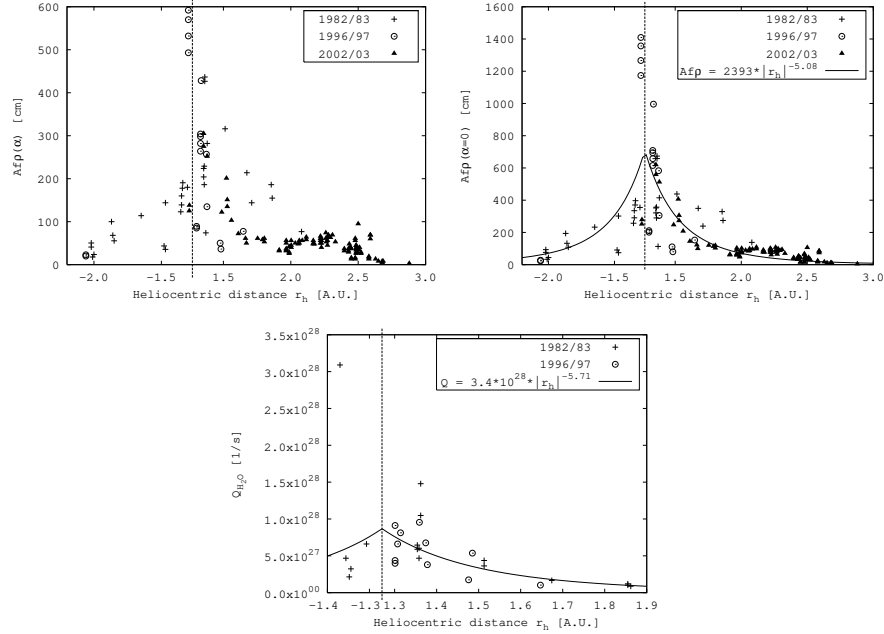


**Fig. 4** Top left: observed  $Af\rho$  values as function of heliocentric distance  $r_h$ . Top right: observed  $Af\rho$  values corrected for phase angle through division by the geometric phase function (Figure 3). Power-law fit for phase angle corrected  $Af\rho$ :  $Af\rho(r_h, \alpha=0) = 2393 \times (r_h/1 \text{ AU})^{-5.08}$  cm. Bottom: Measured  $H_2O$  production rates with corresponding power-law fit  $Q_{H_2O}(r_h) = 3.4 \times 10^{28} \times (r_h/1 \text{ AU})^{-5.71}$  molecules/s.

$Af\rho$  has been measured for 67P/C–G during three perihelion passages (1982/83, 1996/97 and 2002/03) [45, 46, 47, 48, 49, 21, 19, 50, 18]<sup>1</sup>. Figure 4 (top left) shows all published  $Af\rho$  data as function of heliocentric distance. The same values after correction for the phase angle dependence using the geometric phase function (Figure 3) are displayed in Figure 4 (top right) together with a power-law fit to the corrected values. Figure 4 (bottom) shows observed production rates of  $H_2O$  [34, 50, 51, 52] and a power-law fit to the data. The exponents of the derived power laws are untypically steep compared with other comets, and more data of high quality will be needed to confirm them. Both  $Af\rho$  and the  $H_2O$  production rate reach their maxima

<sup>1</sup> The data from these publications are summarised in the data base at [http://berlinadmin.dlr.de/Missions/corot/caesp/comet\\_db.shtml](http://berlinadmin.dlr.de/Missions/corot/caesp/comet_db.shtml). The site also includes data obtained by amateur astronomers.

around 30 days after perihelion. No dust coma was detected beyond at least 4.9 AU [53].

## 2.5 Dust Temperature

Assuming that a particle is characterised by the Bond albedo  $A_B$  at visible wavelengths and the emissivity  $\epsilon$  in the infrared, its temperature  $T$  at the heliocentric distance  $r_h$  (in AU) is given by the equilibrium between absorbed solar and emitted thermal radiation:

$$\frac{(1 - A_B) I_\odot}{r_h^2} = 4 \epsilon \sigma T^4, \quad (3)$$

where  $\sigma$  is the Stefan-Boltzmann constant and  $I_\odot = (1367 \pm 2) \text{ W m}^{-2}$  the solar flux at 1 AU [54]. The resulting equilibrium temperature is

$$T(r_h, A_B, \epsilon) = 278.8 \text{ K} \left( \frac{1 - A_B}{\epsilon} \right)^{\frac{1}{4}} \frac{1}{\sqrt{r_h}}. \quad (4)$$

A blackbody would be characterised by  $A_B = 0$  and  $\epsilon = 1$ . The temperatures of dust in the inner solar system are generally such that the main emission lies in the infrared. In practice, the temperature is derived from fitting a blackbody spectrum to measurements of the brightness at different infrared wavelengths.

The coma of 67P/C-G was monitored at multiple wavelengths in the range of 1 to 20  $\mu\text{m}$  between September 1982 (1.50 AU preperihelion) and March 1983 (1.88 AU postperihelion) [34]. The derived temperatures of the dust in the coma were throughout higher than those of a theoretical blackbody at the same heliocentric distance, which is generally attributed either to the presence of submicron-sized particles (i.e. smaller than the dominant wavelength range of the thermal emission) [34] or to very porous aggregates of small grains [35, 40]. For a given heliocentric distance, the colour temperature was higher post- than pre-perihelion, suggesting a change in the particle properties or in the dominant size. Additionally, an 8- 13- $\mu\text{m}$  spectrum was taken on 23 October 1983. It did not show a silicate feature, which is usually taken as an indication for the dominance of somewhat larger and more compact grains.

Excess colour temperatures were also derived from IRAS observations of cometary trails at 12, 25, and 60  $\mu\text{m}$  [17]. For 67P/C-G, the derived temperature at 2.3 AU was approximately 14% above that of a blackbody at the same heliocentric distance, corresponding to  $\epsilon/(1 - A_B) = 0.6 \pm 0.2$ .

Figure 5 shows the temperature measurements discussed above and – for comparison – the equilibrium temperature of a blackbody as a function of heliocentric distance. The data from the coma [34] and from the trail [17] are

remarkably consistent given that coma and trail are generally assumed to be dominated by different particle populations ( $\mu\text{m}$ - versus mm-cm sized).

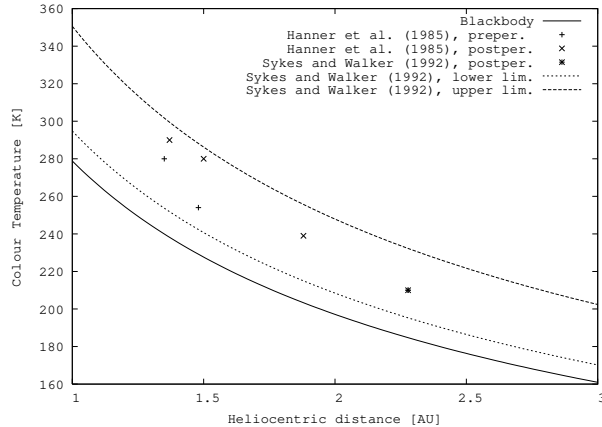


**Fig. 5** Colour temperatures of the dust from 67P/C-G derived from multi-wavelength infrared observations. The symbols “+” and “x” refer to observations of the coma before and after perihelion, respectively [34]. The asterisk indicates the temperature of the dust trail [17], and the two dashed lines correspond – via Equation 4 – to the upper and lower limit of  $\epsilon/(1 - A_B)$  derived from the same data. The solid line shows the temperature of a theoretical blackbody, described by Equation 4 with  $A_B = 0$  and  $\epsilon = 1$ .

## 2.6 Dust Size Distribution

The size distribution of cometary dust has been inferred from both astronomical images and in situ data. While the former yield a *size* distribution, the latter contain information on the *masses* of the particles. For optical images, the determined sizes scale directly with the particle albedo. The conversion from size to mass requires knowledge of the bulk density of the particles.

A mass or size distribution can be specified in the form of either a *differential* or a *cumulative* distribution. The cumulative mass distribution  $F(m_0)$  gives information on the fraction  $N$  of particles that have a mass greater than some mass  $m_0$ :

$$N(m > m_0) = F(m_0). \quad (5)$$

The differential mass distribution  $f(m)$  characterises the relative abundance  $n$  of particles inside a mass interval  $[m_1, m_2]$ :

$$n(m_1 < m < m_2) = \int_{m_1}^{m_2} f(m) dm = F(m_1) - F(m_2). \quad (6)$$

If the mass of a particle can be converted to a size by a relation  $s(m)$ , a corresponding differential size distribution  $g(s)$  exists:

$$\int_{m_1}^{m_2} f(m) dm = \int_{s(m_1)}^{s(m_2)} g(s) ds. \quad (7)$$

It is generally assumed that – at least in intervals of the total mass range covered by cometary dust – the distributions can be approximated by power laws. In the literature, both the exponents  $\gamma$  of the *cumulative mass distribution*  $F(m) \sim m^{-\gamma}$  and  $\alpha$  of the *differential size distribution*  $g(s) \sim s^\alpha$  are commonly used. For a constant bulk density in the concerned size interval we have  $m(s) \propto s^3$  and  $dm \propto s^2 ds$ . Hence the exponents  $\gamma$  and  $\alpha$  are related by

$$\alpha = -3\gamma - 1. \quad (8)$$

The mass distribution at the nucleus is different from the one in the coma because of the size-dependence of the emission velocities. In general, large particles are more abundant in the coma than close to the surface because of their lower speeds. The relation between the size distributions in the coma and at the nucleus may be additionally complicated by fragmentation or evaporation of grains [55, 42, 56] and by an inhomogeneous distribution of surface activity [57].

In situ data on the dust mass distribution were obtained by the dust instruments on board the spacecraft VeGa 1 and 2 and Giotto at comet 1P/Halley in 1986 [55, 58, 42, 57], on board Giotto at comet 26P/Grigg-Skjellerup in 1992 [59], and on board Stardust at comet 81P/Wild 2 in 2004 [60, 56]. The measured quantity is not the mass distribution of dust as released from the nucleus but the cumulative flux or fluence on the concerned instrument. The fluence is defined as the flux integrated over the spacecraft trajectory, it represents therefore an average mass distribution. The flux (or the fluence measured in only sections of the trajectory) showed significant variation with time during both the 1P/Halley and the 81P/Wild 2 fly-bys.

Table 1 lists mass- or size-distribution exponents given in the literature. Still no general agreement has been reached on the interpretation of the data with respect to the dust mass distribution at the nucleus, but the authors listed in Table 1 do agree that the mass of dust in the coma is dominated by the largest emitted particles. The cumulative fluences registered at the various spacecraft show different exponents for large and small particles. The interpretations of this observation are not unanimous, either.

**Table 1** Exponents of the cumulative fluence on a spacecraft,  $\tilde{\gamma}$ , the cumulative mass distribution,  $\gamma$ , and the differential size distribution,  $\alpha$ , compiled from the literature. **Bold** values are taken directly from the publications, the remaining values were derived assuming the following relations. To translate  $\tilde{\gamma}$  to  $\gamma$ , it is assumed that the speeds of small particles are limited by the speed of the gas and therefore independent of size. Hence  $\gamma = \tilde{\gamma}$  for small particles (indicated by “†”). For larger particles, the relation  $v \propto m^{-1/6}$  is used, which was derived from a radially symmetric coma model [43], resulting in  $\gamma = \tilde{\gamma} + 1/6$  for large particles (indicated by “\*”). The relation between the differential size distribution and the cumulative mass distribution is given by  $\alpha = -3\gamma - 1$ . Results from modelling of astronomical images are not included here. For 67P/C-G a compilation of size distributions derived by various authors is shown in Figure 7 (bottom).

Comet	Instrument(s)	Mass/size interval	$\tilde{\gamma}$	$\gamma$	$\alpha$	Ref.
1P/Halley	DIDSY&PIA	$10^{-13} \dots 10^{-8}$ kg		<b>1.02</b>	-4.06	[55]
		$10^{-8} \dots 10^{-6}$ kg		<b>0.71</b>	-3.13	
	DIDSY&PIA	$10^{-19} \dots 2 \times 10^{-14}$ kg	<b>0.18</b>	0.18†	-1.54	[58]
		$2 \times 10^{-14} \dots 10^{-6}$ kg	<b>0.94</b>	1.11*	-4.32	
	VeGa 1	$10^{-19} \dots 10^{-12}$ kg	<b>0.26</b>	0.26†	-1.78	
		$10^{-12} \dots 10^{-9}$ kg	<b>1.19</b>	1.36*	-5.07	
	VeGa 2	$10^{-19} \dots 1.6 \times 10^{-13}$ kg	<b>0.26</b>	0.26†	-1.78	
$1.6 \times 10^{-13} \dots 10^{-9}$ kg		<b>0.90</b>	1.07*	-4.2		
	DIDSY	> 20 $\mu$ m			-3.5 $\pm$ 0.2	[57]
26P/G-S	DIDSY/GRE	$10^{-9} \dots 10^{-7}$ kg	<b>0.27</b> <sup>+0.13</sup> <sub>-0.20</sub>	0.44*	-2.3	[59]
81P/Wild 2	DFMI	$10^{-14} \dots 10^{-9}$ kg	<b>0.85 <math>\pm</math> 0.05</b>	1.02*	-4.05 $\pm$ 0.15	[56]
	Stardust Samples	$10^{-17} \dots 10^{-3}$ kg	<b>0.57</b>	0.74*	-3.21	[61]

## 2.7 Radiation Pressure

Both solar gravity and the radiation pressure force are inversely proportional to the heliocentric distance squared, and point radially away from the Sun. Radiation pressure can, therefore, be included in the equation of motion of a particle by introducing a modified potential substituting the gravitational constant,  $G$ , by  $\tilde{G} = G(1 - \beta)$ , where  $\beta$  stands for the ratio of solar gravity to the radiation pressure force. It depends only on material properties of the dust grains, not on their distance from the Sun:

$$\beta = \frac{3 L_{\odot}}{16 \pi c G M_{\odot}} \frac{Q_{\text{pr}}}{\rho s}. \quad (9)$$

$L_{\odot}$  and  $M_{\odot}$  are the luminosity and mass of the Sun, and  $c$  is the speed of light. The grain has the bulk density  $\rho$  and the effective radius  $s$ , and it is characterised by the radiation pressure efficiency  $Q_{\text{pr}}$  [62, 43].  $Q_{\text{pr}}$  represents

the absorption and scattering properties of the grain averaged over the solar spectrum. For homogeneous spheres and some other simple shapes,  $Q_{\text{pr}}$  can be calculated in an exact way from the complex refractive index of the material [63, 64]. For more complicated structures, a variety of theoretical and experimental approaches exist to obtain  $Q_{\text{pr}}$  [65]. While for particle sizes on the order of 0.01 to 1  $\mu\text{m}$ ,  $\beta$  depends sensitively on material, shape, structure, surface properties, and size of the particles, it is approximately constant for much smaller particles, and proportional to  $1/(\rho s)$  for large ones, i. e. in the geometric optics regime. This implies that for sub-millimetre and larger particles,  $Q_{\text{pr}}$  is to first order independent of size [62, 64].

### 3 Results of Modelling the 67P Dust Tail and Trail

In this Section, we give an overview of the efforts undertaken to derive properties of the 67P/C-G dust from modelling astronomical observations of the thin, bright feature described in Section 2.2, variably referred to as neckline, antitail, or trail. The main quantities to be constrained by the models are the dust size distribution, the radiation pressure efficiency, and the emission speeds. The derived values will serve as input to the hydrodynamic coma model used in Section 4 to predict the dust environment inside the coma. In the following, we summarise the results from neckline photometry applied to images taken in 2002/03 [22, 23], from analysis of the antitail as observed in May 2003 [66], and from simulations of the dust trail in visible and infrared wide-field observations between 2002 and 2006 [25, 26, 27].

The position of a dust particle in a cometary tail is a function of the radiation pressure coefficient  $\beta$ , the emission time, and the emission speed; and  $\beta$  is closely related to the mass of a particle. Hence, the effect of solar radiation pressure is similar to that of a mass spectrometer. To understand the formation of dust tails, the concept of synchrones and syndynes was introduced by Bredikhin [67]. Synchrones are the positions of particles of different  $\beta$  emitted at a given time, while syndynes describe the positions of particles of fixed  $\beta$  and varying emission time. Both terms refer to hypothetical particles emitted with zero velocity relative to the nucleus. Since, realistically, the initial velocity of a dust grain is different from zero, the resulting synchrone or syndyne will have a finite cross section with a radius proportional to the product of dust emission speed and time elapsed since emission. In particular, grains released at a given time with isotropic speed will form a spherical shell the centre of which moves along the appropriate syndyne.

This description was used by Finson and Probstein [1, 68] to derive properties of the dust size distribution from the brightness patterns observed in cometary dust tails. Their method is limited to recently emitted and small particles, because it neglects tidal effects and others (e.g. direction-dependent emission speed or production rate) that cause a dust shell to divert from the

spherical shape [11, 69, 13]. Various approaches to surmount these limitations are described in the following.

### 3.1 Neckline Photometry

Fulle et al. [22] analyse 67P/C-G images obtained in March 2003 ( $r_h = 2.6$  AU) and before, when the comet was active and exhibited a significant coma. They employ both an analytical theory of neckline photometry and an inverse Monte Carlo model.

The former is an analytical method to infer the emission speeds and abundance of particles as a function of the radiation pressure parameter  $\beta$  [70]. It is applied to an image of the comet obtained with the Schmidt Telescope at the Thüringer Landessternwarte (TLS) in Tautenburg on 27-28 March 2003. The method relies on the assumption that the bright narrow feature in the tail is a neckline, and that all intensity observed in this feature is due to dust emitted within an interval of 10 hours at a true anomaly of  $180^\circ$  before that of the observation, which corresponds to 5 May 2002 (105 days before perihelion) and  $r_h = 1.8$  AU. The authors find that – in this particular time interval – both the mass and the cross section of dust emitted by the comet were dominated by particles in the size range of 1.5 to 10 mm, and that the exponent of the differential size distribution,  $\alpha$ , was between -3.5 and -3. From the fact that the described feature had been constantly observable since perihelion in August 2002, they infer that the characteristics of the dust emission as recorded in the neckline did not change between 3.6 and 1.7 AU before perihelion.

The second method – the inverse Monte Carlo model – consists in a least-squares fit of simulated images to the measured surface intensity [71]. This method yields a set of time-dependent dust parameters (size distribution, emission velocity, size range,  $Af\rho$ , and dust production rate). The obtained solution is unique in the mathematical sense of a least-squares fit; its physical probability remains harder to evaluate. The method is applied to an image obtained with the Telescopio Nazionale Galileo (TNG) on La Palma during the same night as the TLS image. Quantitative interpretation of the model is achieved through matching of the modelled  $Af\rho$  to the value measured during a different observation close in time [49]. The authors [22] conclude that the time dependence of all parameters must be asymmetric with respect to perihelion in order to match the observation. The size distribution exponent drops from  $-3.5$  before to  $-4.5$  after perihelion, the mass loss rate from 200 kg/s to 10 kg/s. The emission speeds decrease by a factor of three during this time interval (from 3 m/s to 1 m/s for a particle of 1 mm radius), and the dominant size by two orders of magnitude. Fulle et al. [22] suggest the existence of two different source regions: one emitting large particles and only

active before perihelion, and one emitting mostly small particles becoming active after perihelion.

A decreasing production rate was also found by Moreno et al. [23] applying a similar method to the same image after calibration.

### 3.2 Antitail Analysis in the Hypersonic Approximation

The dust size distribution has been evaluated by analysis of the brightness profile along the 67P/C-G tail using the Finson-Probstein model in the *hypersonic approximation* [66], which was applied to an image (Figure 1) obtained with ESO/VLT on 3 May 2003 [19, 20].

At the time of the observation, 67P/C-G was at a heliocentric distance of 2.9 AU postperihelion. A plot of synchrones and syndynes (Figure 6) shows that all synchrones corresponding to ejection before 1.5 AU postperihelion (23 October 2002) appear projected in the direction towards the Sun, forming an antitail. They all are – in projection – inclined against the neckline by less than  $0.8^\circ$ , which places doubts upon the assumption that all dust in the bright feature was emitted during an interval of merely 10 hours, on which the first model described in Section 3.1 relies [22].

The hypersonic approximation holds when the extent of the dust shells along a synchrone is small, such that a unique relation between the position

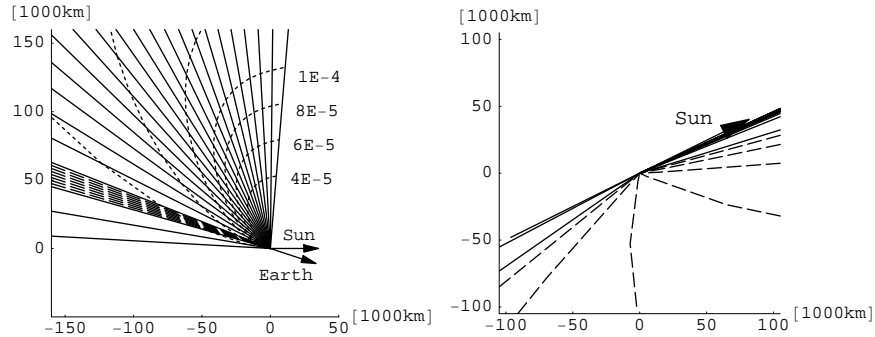


**Fig. 6** For 3 May 2003 synchrones are shown projected in the comet orbit plane (top) and image plane (bottom). The solid lines correspond to synchrones ejected in steps of  $10^\circ$  in true anomaly starting  $5^\circ$  in true anomaly before the observation time back to an ejection time that corresponds to a heliocentric distance of 3 AU before perihelion. Synchrones corresponding to ejection times after mid January 2003 appear in the direction opposed to the Sun. The synchrones of particles ejected before mid December 2003 appear in Sun direction. Only the synchrones of particles ejected in between (shown as long dashed) have significant angles with the Sun or anti-sun direction. Projected in the comet orbit plane (top panel) also syndynes are shown (dashed). The  $\beta$ -values corresponding to the syndynes are annotated for the larger particles. The  $\beta$  values of the smaller particles are  $1.5 \times 10^{-4}$ ,  $3 \times 10^{-4}$ , and  $1 \times 10^{-3}$ .



on the synchrone and  $\beta$  can be assumed [1]. It is then possible to infer the size distribution of the particles ejected from the nucleus from the brightness profile along the synchrone, if one of the following two conditions is met: (1) Either the antitail originates from the superposition of many synchrones that – in projection – have only a small offset from each other compared with the extension of the dust shells perpendicular to the synchrone. Or (2) the brightness along one direction in the image plane is dominated by one synchrone alone. A generalisation of the original formulation of the hypersonic approximation [1] – which applied only to spherical shells – has been developed for tidally distorted elliptical shells, assuming radially symmetric particle emission [66].

The intensity along the antitail on 3 May 2003 could be fitted by a power law with an exponent of  $-0.4$ , which was translated to  $\alpha = -4.1$  for the differential size distribution between at least 3 AU before and 1.5 AU after perihelion in 2002 [66]. To put this result in a wider context, we have compared the measured brightness distribution along the antitails of different comets rather than the derived size distributions, because we found that different authors use different models to derive the size distribution from the measured brightness exponent. We found that the brightness variation measured for the antitail of 67P/C–G is rather typical compared with the antitails of other comets, such that also the dust size distribution of 67P/C–G may be typical.

### 3.3 Trail Analyses

Several wide field images of the dust along the orbit of 67P/C–G were obtained between 2002 and 2006 in both optical and infrared light, and their analyses are summarised in the following.

Three images – one optical and two infrared at  $24\ \mu\text{m}$  – with fields of view of about half a degree were analysed using a generalised Finson-Probstein approach that takes into account the tidal deformation of dust shells on long time-scales [25]. The optical image was obtained in April 2004 with the Wide Field Imager at the ESO/MPG 2.2m telescope on La Silla at  $r_h = 4.7$  AU (Figure 2), and the infrared images were taken by the MIPS instrument on board the Spitzer Space Telescope of NASA in August 2005 and April 2006 ( $r_h = 5.7$  AU in both cases). All three images were thus taken when the comet was close to aphelion and not active, such that no particles larger than approximately  $100\ \mu\text{m}$  are expected to be present in the fields of view. Simulated images were generated taking into account dust emitted during all seven perihelion passages since the last close encounter with Jupiter in 1959. The time-dependence of the dust production was modelled on the observed time-dependence of  $Af\rho$ . The emission speeds and surface activity were assumed to be isotropic, and the relative dependence of the emission speeds

on size and heliocentric distance was obtained by help of the hydrodynamic coma model described in Section 4 of this article, and from the observed time-dependence of the water production rate. Within this framework, the parameter values found most suitable to reproduce both the brightness profile along the trail and its width were the following: The emission speeds of a 1 mm radius particle at perihelion ranged from 6 m/s to 12 m/s, decreasing by a factor of 10 until 3 AU. The size dependence of  $\beta$  could be characterised by Equation 9 with  $Q_{\text{pr}}/\rho$  between 1 and 3 cm<sup>3</sup>/g, which – assuming  $Q_{\text{pr}} = 1$  for large particles – corresponds to bulk densities between 0.3 and 0.9 g/cm<sup>3</sup>. The size distribution exponent for particles larger than 100  $\mu\text{m}$  was in the range of -4.1 to -3.9. In order to reproduce both the optical and the infrared images, a geometric albedo for visible light of  $p = 4\%$  was required if the dust was assumed to be emitting as a blackbody ( $\epsilon = 1$  in Equation 4), but  $p = 10\%$  if  $\epsilon/(1 - A) = 0.6$  [34, 17]. Lower limits for the production rates of particles with  $s > 100 \mu\text{m}$  ranged from 100 kg/s at perihelion to 0.2 kg/s at 3 AU, corresponding to  $Af\rho$  values of 4 and 0.05 m, respectively. This implies that particles larger than 100  $\mu\text{m}$  would have contributed at least 50% of the total  $Af\rho$  observed while the comet was in the inner solar system, which is difficult to reconcile with the size distribution exponent on the order of -4.

Three optical images (R-band) were obtained between September 2002 and February 2003 with the 1.05-m Schmidt telescope of the Kiso Observatory at Nagano, Japan [26]. The difference in position angle of freshly emitted dust and the trail (dust from previous apparitions) was 1° or larger in these images, thus – in contrast to images taken at later dates – a clear separation of both dust populations is possible. Taking into account dust emitted after aphelion in 1986 and assuming  $p = 4\%$ ,  $\rho = 1 \text{ g/cm}^3$ , and  $Q_{\text{pr}} = 1$ , the images were best reproduced by a model with cone-shaped emission with a half opening angle between 45° and 90°, a size distribution exponent of -3.5 with particles in the range between 6  $\mu\text{m}$  and 5 mm, and dust production rates of about 200 kg/s at perihelion and 15 kg/s at 3 AU. The emission speeds were assumed to be proportional to  $s^{-1/2}$  and  $r_{\text{h}}^{-1/2}$ , absolute values for a 1 mm particle ranging from 8 to 18 m/s at perihelion and from 5 to 12 m/s at 3 AU.

Two further observations were analysed by help of a Monte Carlo model [27]: an optical image (Gunn r' filter) obtained in June 2003 with the 5-m Hale telescope at Palomar Observatory, and an infrared (24  $\mu\text{m}$ ) image made with Spitzer/MIPS in February 2004. The trail of particles from previous perihelion passages was not detected in the Palomar image, but was visible to Spitzer. The applied model includes the assumptions of  $Q_{\text{pr}} = 1$ ,  $\rho = 1 \text{ g/cm}^3$ , dust production rates  $Q_{\text{d}} \propto r_{\text{h}}^{-5.8}$ , and emission speeds  $v \propto \sqrt{\beta/r_{\text{h}}}$ . Particles larger than 0.5  $\mu\text{m}$  and emitted after March 1993 were included in the analysis. The images were best fitted by a cosine-shaped distribution of the surface activity, peaking at the subsolar point, and a differential size distribution exponent of -3.5. The emission speeds of a 1 mm particle at the subsolar point varied between 10 m/s at perihelion and 7 m/s at 3 AU.

### 3.4 Summary of Modelling Results

Figure 7 summarises the dust production rates, emission speeds and size distributions derived by help of the various models described in Sections 3.1 to 3.3. We wish to stress that – with the exception of the TNG image obtained in March 2003 – each model has been applied to a different set of images, and each model was able to reproduce the images that were analysed by it. However, the ranges of parameter values derived from the different models are considerable, such that it is at present difficult to derive a consistent picture of the CG dust environment on the basis of these results. Future work on this matter should focus on finding a set of parameters that is able to reproduce all available observations of the CG tail and trail.

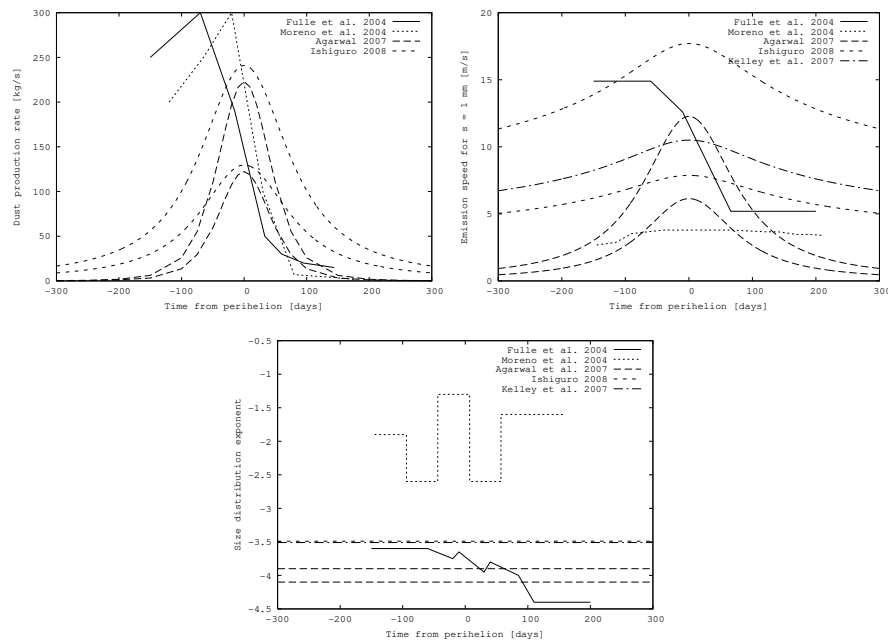


**Fig. 7** Comparison of dust characteristics derived from the different models described in Section 3. Two lines of the same style represent upper and lower limits. Top left: dust production rates. Top right: emission speeds of a dust grain with 1 mm radius. For anisotropic models, the peak emission speed (assumed above the subsolar point) is given. Bottom: Exponents of the differential size distribution.

## 4 Dust Environment Model and Predictions for 67P/C-G

In this section, the state of dust in the coma of 67P/C-G is predicted by means of a hydrodynamic model [7, 8, 9, 10]. Three emission scenarios and three size distribution exponents are studied, and estimates of the fluxes on a spacecraft for several types of trajectory and the radiation environment in the coma are presented.

### 4.1 Coma Model and Parameters

The employed model can be considered as the simplest possible physically consistent model of the inner coma: The comet nucleus is assumed to be of spherical shape, and the activity distribution on its surface is axis-symmetric with respect to the comet-Sun line. The flows of gas and dust around the comet are calculated rendering at any position in the coma the gas density, velocity, and temperature, and the number density and velocity of dust particles of different mass classes. Each class represents particles having masses within one decade in the range of  $10^{-20}$  to  $10^4$  kg. All dust particles of one class are assigned the same representative mass and radius. It is assumed that the particles have spherical shapes and a constant bulk density of  $1000 \text{ kg/m}^3$ .

The numerical method used to compute the dynamics of gas and dust takes advantage of the fact that the influence of the dust on the gas flow is of minor importance. In a first step, the gas flow is calculated without taking into account the presence of dust. In a second step, dust trajectories are integrated considering the gravitation of the nucleus and the gas drag force.

The gas flow is calculated under the assumptions that the gas is in thermal equilibrium everywhere, and that the mean molecular mass is constant across the coma. It is given by the mean of the masses of the two most common molecules,  $\text{H}_2\text{O}$  and  $\text{CO}$ , weighted by their overall abundances in the coma. The production rates of these species are input parameters to the model. To first order, the CO-activity can be treated as independent of heliocentric distance, and the constant value of  $10^{26}$  molecules/s is adopted for 67P/C-G. An upper limit for the CO-production of  $10^{27}$  molecules/s at 3 AU has been inferred from radio observations [72]. The water activity is assumed to vary with heliocentric distance and time as indicated by observations (Figure 4, bottom). The dust activity is scaled such that the observed  $Af\rho$  is reproduced for the employed size distribution and albedo.

Since, at present, the size distribution estimates vary considerably (Section 3.4), we consider in the following the same range of mass distributions as in earlier models for 46P/Wirtanen [7]: two “extreme” and a “nominal” one.

All are characterised by different exponents for light and heavy particles, and the analytical form used for the cumulative mass distribution is as follows [58]:

$$F(m) = \left( \frac{(1+x)^{b-1}}{x^b} \right)^{ac} \text{ with } x = \left( \frac{m}{m_t} \right)^{1/c}. \quad (10)$$

This function is specified by the positive parameters  $a$ ,  $b$ ,  $c$ , and  $m_t$ . The exponent  $-\gamma$  of the cumulative mass distribution tends towards  $-a$  for heavy particles ( $m \ll m_t$ ) and towards  $-ab$  for light ones.  $m_t$  is the mass where the transition between the two exponents takes place, and  $c$  determines the sharpness of the transition. The three mass distributions considered in this paper are different only by their slopes for heavy particles. For light particles we use  $\gamma = ab = 0.26$  throughout (corresponding to  $\alpha = -1.8$ ), for the transition mass  $m_t = 10^{-13}$  kg, and  $c = 2$ . The slopes for large particles are as follows: the (velocity-corrected) fit to the fluence measured on Giotto [58] gave  $\alpha = -4.3$  ( $\gamma = 1.1$ ) which we use as one of the “extreme” distributions. From the same data, an exponent in the range of  $\alpha \in [-3.7, 3.3]$  has been derived [57], wherefore we adopt  $\alpha = -3.7$  ( $\gamma = 0.9$ ) as the “nominal” and  $\alpha = -3.3$  ( $\gamma = 0.8$ ) as the other “extreme” distribution. It must, however, be emphasised that for  $\alpha > -3.5$ , the observed brightness is dominated by light scattered by large particles [7]. Figure 8 show different moments of the mass distribution.

In the following, model predictions are given for several heliocentric distances: the perihelion distances in 2015 ( $r_h = 1.24$  AU) and 2002 ( $r_h = 1.29$  AU), and 1.87 AU, 2.5 AU, and 3 AU. The values used for the water production rate, for  $Af\rho$ , and for the phase angle  $\alpha$  are listed in Table 2. We use a geometric albedo of 4% and the phase function shown in Figure 3. While the production of CO is assumed to be isotropic, for the release of H<sub>2</sub>O three different surface activity distributions are taken into account. The first represents a homogeneously composed surface such that the strength of gas production is determined by the amount of solar energy received by a given surface element (*insolation driven model*). In the second scenario, a *jet* is simulated describing the surface activity by a Gaussian profile centred at the subsolar point [57, 73]. This model is expected to yield upper limits for local quantities inside a jet, while the insolation driven model gives estimates

**Table 2** Water production rates  $Q_{\text{H}_2\text{O}}$ ,  $Af\rho$ -values and phase angles  $\alpha$  for those heliocentric distances  $r_h$  used to obtain the model predictions in this section.

$r_h$ [AU]	$Q_{\text{H}_2\text{O}}$ [molecules/s]	$Af\rho(\alpha)$ [cm]	$\alpha$ [deg]
1.24	$1.3 \times 10^{28}$	400	35
1.29	$1.0 \times 10^{28}$	300	35
1.87	$1.2 \times 10^{27}$	65	32
2.5	$1.8 \times 10^{26}$	20	5
3.0	$6.4 \times 10^{25}$	5.8	19

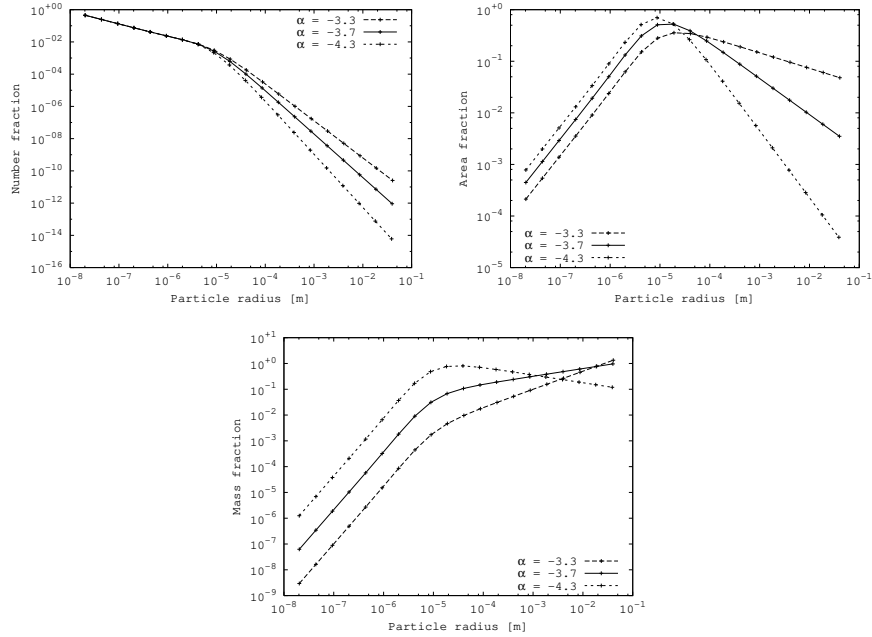


**Fig. 8** Different moments of the mass distributions studied in Section 4. Top left: number fraction. Top right: area fraction. Bottom: mass fraction. To convert mass to radius, a bulk density of  $\rho = 1000 \text{ kg/m}^3$  was assumed.

for quantities averaged over time and space. In addition, an even simpler *radially symmetric model* is used in which the water activity is distributed equally over the comet surface.

The average radius of the nucleus of 67P/C-G as given in the literature is in the range of 1.7..3.2 km [74, 75, 76, 77, 78, 53, 27]. The geometric albedo of the nucleus in R-band is in the range of 0.045 to 0.06, and the bulk density of the nucleus is estimated to  $370 \text{ kg/m}^3$  [78]. The following results were obtained for a spherical nucleus having a radius of 2 km and a geometric albedo of 4%.

## 4.2 Dust Terminal Speeds

The terminal speeds of dust as a function of particle size for the three different emission scenarios are shown in Figure 9. For comparison, the corresponding values for comet 46P/Wirtanen, the former Rosetta target, are shown as well. Note that all curves are at perihelion, hence the comets are compared at different heliocentric distances. While the terminal speeds for 46P/Wirtanen

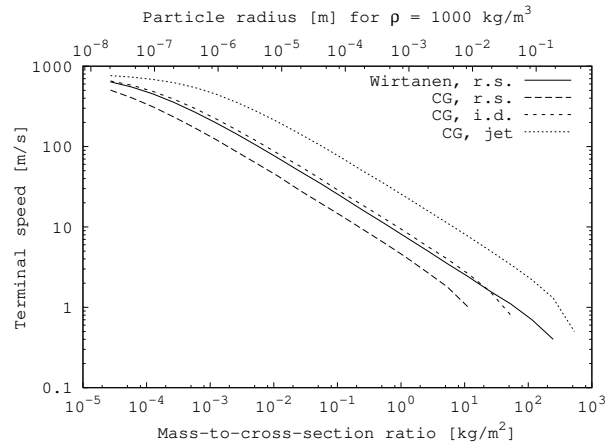


**Fig. 9** Terminal speeds as functions of mass-to-cross-section ratio for various emission scenarios (r.s.: radially symmetric, i.d.: insolation driven). The corresponding particle radii for a bulk density of  $\rho = 1000 \text{ kg/m}^3$  are indicated at the upper margin. Values for 67P/C–G are given at 20 km from the nucleus centre above the subsolar point and at perihelion ( $r_h = 1.29 \text{ AU}$ ). For 46P/Wirtanen they are at 10 km from the nucleus centre and at the perihelion distance of  $r_h = 1.06 \text{ AU}$ .

are given at 10 km from the nucleus centre, those for 67P/C–G are at 20 km, because the dust particles have not quite reached their terminal speeds at lower heights.

In the radially symmetric models, the terminal speeds are higher in the case of 46P/Wirtanen than of 67P/C–G. The reason is that both comets have similar gas production rates although 46P/Wirtanen is smaller. Hence the gas directly over the surface is denser and the dust reaches higher velocities. The ratio between the speeds expected for 67P/C–G and 46P/Wirtanen in the radially symmetric model ranges from 0.8 for small particles to 0.5 for large ones. The speeds shown in Figure 9 were computed for a dust bulk density of  $\rho = 1000 \text{ kg/m}^3$ . Scaling to other particle densities can to first order be done assuming that particles with the same cross section to mass ratio reach the same velocities. For the larger particles, a power law of the following form was fitted to the calculated speeds:

$$v(s) = v_0 \left( \frac{s}{s_0} \right)^{-d}, \quad (11)$$

with  $s_0 = 1 \text{ mm}$ . The resulting parameters for the different scenarios are given in Table 3. For the fits, all dust classes with particle radii  $s > 0.1 \text{ mm}$  have been used. The class with the largest liftable particles was not included because of the strong influence of the gravitation of the comet. For 46P/Wirtanen, the exponent  $d$  is closer to the expected value of 0.5 than for 67P/C–G because of the latter’s larger nucleus and resulting stronger gravity.

**Table 3** Results of fitting a power law to the dust terminal speeds for large particles above the subsolar point at perihelion. Values are given for different emission models: radially symmetric (r.s.), insolation driven (i.d.), and jet model.

Model	$r_h$ [AU]	$v_0$ [m/s]	Exponent $d$
Wirtanen r.s.	1.06	7.0	0.51
C-G r.s.	1.29	3.9	0.53
C-G i.d.	1.29	8.0	0.53
C-G jet	1.29	22.2	0.52

### 4.3 Dust Flux at 1.29 AU

Here we give numerical values for the fluxes of gas and dust on a surface directed towards the nucleus at 20 km from the nucleus centre above the subsolar point for various mass distributions and emission scenarios. As the speeds of gas and dust outside the acceleration zone are almost constant, the fluxes there can be scaled by an inverse square law. Note that the values given for the gas are only valid as long as the gas is cold, i.e. far from the nucleus. Within a few comet radii from the surface, the velocity distribution of the gas should be taken into account. Consequently, there will also be a flux on surfaces which are directed away from the flux direction. The numerical values are given in the appendix of [66] and visualised in Figure 10. The number and mass fluxes (upper panels Figure 10) in are relevant for different sensors of the GIADA instrument. The lower left panel shows the surface coverage by dust which is important for estimating thermal effects on spacecraft and instruments. The lower right panel describes the momentum transfer onto the spacecraft by the dust.

### 4.4 Dust Collection along Sample Spacecraft Trajectories

During most of the mission, regions of strong dust emission in the coma will be avoided, because impacts of dust particles constitute a hazard to the Rosetta spacecraft. This hazard includes damage of sensitive surfaces by cratering and erosion due to high velocity dust impacts, contamination of surfaces and modification of their optical and thermal properties due to sticking of dust, and even mechanical blockage of gears and hinges by larger grains. This hazard has been taken into account in the design of the Rosetta spacecraft and its instruments, e.g. by painting the spacecraft black so that sticking dust will not significantly change the thermal properties of the spacecraft, and by employing movable shutters in front of sensitive surfaces such as cameras. Nevertheless, in the vicinity of the comet, spacecraft operations



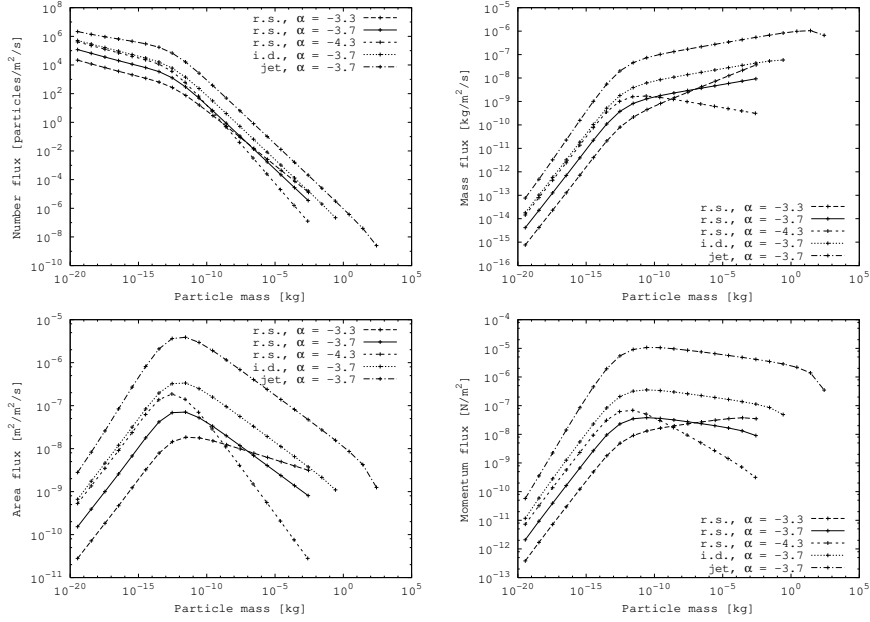


**Fig. 10** Fluxes over particle mass for various mass distributions and emission geometries. Top left: number flux, top right: mass flux, bottom left: area flux, bottom right: momentum flux.

will keep exposure to dust to a minimum [79]. In order to fulfil the dust collection requirements of the COSIMA and MIDAS instruments the spacecraft occasionally will have to pass through regions of high dust density. The design of these passages will depend on the collection requirements of the dust instruments.

For simple dust collection trajectories, the surface coverage by dust (assuming all dust sticks to the surface) has been calculated for the different dust emission scenarios and mass distributions described in Section 4.1. The considered trajectory types are one revolution on a circular orbit, a parabolic orbit, and a straight line trajectory passing the nucleus at a speed  $v = 1$  m/s. All trajectories are assumed to pass at closest approach ( $r_{CA} = 4$  km from the nucleus centre) over the subsolar point, i.e. the region of highest dust density in our model. The fraction of the surface covered by dust after one passage of the nucleus is given in Table 4. For other closest approach distances the surface coverage levels scale with  $r_{CA}^{-0.5}$  for Keplerian orbits (circles and parabola) and with  $r_{CA}^{-1}$  and  $v^{-1}$  for straight line passages. The values in Table 4 refer to different dust production rates, i.e. different heliocentric distances.

A surface coverage of one implies roughly a mono-layer of differently sized dust grains, most of which are grains in the 1 to 10  $\mu\text{m}$  size range (cf. Figure 8,

top right). Since the dust instruments are sensitive to different sizes of dust grains it is useful to determine the dust coverage by particles above a certain minimum size. This is achieved by applying the scaling factors for different minimum dust sizes given in Table 5. Useful surface coverage levels of dust collectors range from  $10^{-4}$  to  $10^{-2}$ , i.e. a  $1 \text{ cm}^2$  collection surface will contain approximately 100 to  $10^4$  particles of  $10 \mu\text{m}$  in size. According to Table 5 these particles constitute about 50% of the covered surface (for the size distribution with  $\alpha = -3.7$ ). The other half of the covered surface consists of more finely dispersed smaller grains.

The COSIMA instrument is sensitive to dust grains of  $10 \mu\text{m}$  and has 23 individual collectors. The MIDAS instrument is sensitive to submicron-sized dust grains and has 60 individual collectors. The exposure of these collectors to the cometary dust flux and the collection of sufficient numbers of dust particles will at the same time lead to significant dust coverage of all spacecraft surfaces facing the comet. During one dust collection passage of Rosetta at large heliocentric distances (2.5 and 3 AU) an individual dust collector may reach only a total dust coverage of approximately  $2 \times 10^{-3}$  and

**Table 4** Total surface coverage of the nucleus-directed side of the spacecraft due to dust particles of all sizes. The table lists the surface coverage for different heliocentric distances and different kinds of orbits. At heliocentric distances of 2.5 and 3 AU the water production rate is comparable with the background CO production rate, therefore, dust emission in form of a jet is not considered. We expect that at these heliocentric distances particles on the order of  $100 \mu\text{m}$  can still leave the comet. All orbits have the point of closest approach to the nucleus over the subsolar point with a distance  $r_{\text{CA}} = 4 \text{ km}$  from the nucleus centre. The considered types of orbits are a parabola, a straight line at constant speed of  $1 \text{ m/s}$ , and a circle. For the parabola and the circle only the part of the trajectory over the comet day side is taken into account.

Model	Orbit	Size distr. exp.	$r_h$ [AU]				
			1.24	1.29	1.87	2.5	3.0
radial sym.	circle	-3.3	0.101	0.075	0.006	0.0008	0.0004
		-3.7	0.272	0.204	0.015	0.0015	0.0005
		-4.3	0.539	0.404	0.030	0.0028	0.0009
insol. driven	parabola	-3.3	0.189	0.142	0.017	0.0016	0.0005
		-3.7	0.606	0.455	0.035	0.0026	0.0007
		-4.3	1.213	0.909	0.062	0.0042	0.0010
	straight line	-3.3	0.148	0.111	0.013	0.0013	0.0004
		-3.7	0.473	0.355	0.027	0.0021	0.0006
		-4.3	0.945	0.709	0.048	0.0034	0.0009
jet	parabola	-3.3	0.917	0.688	0.106		
		-3.7	3.540	2.655	0.249		
		-4.3	6.896	5.172	0.421		
	straight line	-3.3	0.685	0.514	0.079		
		-3.7	2.644	1.983	0.185		
		-4.3	5.153	3.865	0.313		

**Table 5** Fraction of area flux due to particles greater than mass  $m_{\min}$  or radius  $s_{\min}$  for the different mass distributions.

$m_{\min}$ [kg]	$s_{\min}$ [m]	$\alpha = -3.3$	$\alpha = -3.7$	$\alpha = -4.3$
$1.000 \times 10^{-20}$	$1.337 \times 10^{-08}$	$1.000 \times 10^{+00}$	$1.000 \times 10^{+00}$	$1.000 \times 10^{+00}$
$1.000 \times 10^{-19}$	$2.879 \times 10^{-08}$	$9.998 \times 10^{-01}$	$9.996 \times 10^{-01}$	$9.992 \times 10^{-01}$
$1.000 \times 10^{-18}$	$6.204 \times 10^{-08}$	$9.993 \times 10^{-01}$	$9.984 \times 10^{-01}$	$9.972 \times 10^{-01}$
$1.000 \times 10^{-17}$	$1.337 \times 10^{-07}$	$9.979 \times 10^{-01}$	$9.955 \times 10^{-01}$	$9.921 \times 10^{-01}$
$1.000 \times 10^{-16}$	$2.879 \times 10^{-07}$	$9.945 \times 10^{-01}$	$9.880 \times 10^{-01}$	$9.788 \times 10^{-01}$
$1.000 \times 10^{-15}$	$6.204 \times 10^{-07}$	$9.855 \times 10^{-01}$	$9.683 \times 10^{-01}$	$9.438 \times 10^{-01}$
$1.000 \times 10^{-14}$	$1.337 \times 10^{-06}$	$9.618 \times 10^{-01}$	$9.166 \times 10^{-01}$	$8.524 \times 10^{-01}$
$1.000 \times 10^{-13}$	$2.879 \times 10^{-06}$	$9.039 \times 10^{-01}$	$7.959 \times 10^{-01}$	$6.512 \times 10^{-01}$
$1.000 \times 10^{-12}$	$6.204 \times 10^{-06}$	$7.971 \times 10^{-01}$	$5.958 \times 10^{-01}$	$3.771 \times 10^{-01}$
$1.000 \times 10^{-11}$	$1.337 \times 10^{-05}$	$6.620 \times 10^{-01}$	$3.897 \times 10^{-01}$	$1.703 \times 10^{-01}$
$1.000 \times 10^{-10}$	$2.879 \times 10^{-05}$	$5.310 \times 10^{-01}$	$2.379 \times 10^{-01}$	$6.782 \times 10^{-02}$
$1.000 \times 10^{-09}$	$6.204 \times 10^{-05}$	$4.201 \times 10^{-01}$	$1.408 \times 10^{-01}$	$2.565 \times 10^{-02}$
$1.000 \times 10^{-08}$	$1.337 \times 10^{-04}$	$3.302 \times 10^{-01}$	$8.245 \times 10^{-02}$	$9.514 \times 10^{-03}$
$1.000 \times 10^{-07}$	$2.879 \times 10^{-04}$	$2.576 \times 10^{-01}$	$4.822 \times 10^{-02}$	$3.528 \times 10^{-03}$
$1.000 \times 10^{-06}$	$6.204 \times 10^{-04}$	$2.001 \times 10^{-01}$	$2.813 \times 10^{-02}$	$1.298 \times 10^{-03}$
$1.000 \times 10^{-05}$	$1.337 \times 10^{-03}$	$1.545 \times 10^{-01}$	$1.637 \times 10^{-02}$	$4.787 \times 10^{-04}$
$1.000 \times 10^{-04}$	$2.879 \times 10^{-03}$	$1.181 \times 10^{-01}$	$9.518 \times 10^{-03}$	$1.773 \times 10^{-04}$
$1.000 \times 10^{-03}$	$6.204 \times 10^{-03}$	$8.923 \times 10^{-02}$	$5.508 \times 10^{-03}$	$6.523 \times 10^{-05}$
$1.000 \times 10^{-02}$	$1.337 \times 10^{-02}$	$6.637 \times 10^{-02}$	$3.167 \times 10^{-03}$	$2.395 \times 10^{-05}$
$1.000 \times 10^{-01}$	$2.879 \times 10^{-02}$	$4.813 \times 10^{-02}$	$1.796 \times 10^{-03}$	$8.815 \times 10^{-06}$
$1.000 \times 10^{+00}$	$6.204 \times 10^{-02}$	$3.366 \times 10^{-02}$	$9.940 \times 10^{-04}$	$3.204 \times 10^{-06}$
$1.000 \times 10^{+01}$	$1.337 \times 10^{-01}$	$2.214 \times 10^{-02}$	$5.256 \times 10^{-04}$	$1.143 \times 10^{-06}$
$1.000 \times 10^{+02}$	$2.879 \times 10^{-01}$	$1.300 \times 10^{-02}$	$2.531 \times 10^{-04}$	$3.844 \times 10^{-07}$
$1.000 \times 10^{+03}$	$6.204 \times 10^{-01}$	$5.748 \times 10^{-03}$	$9.349 \times 10^{-05}$	$1.035 \times 10^{-07}$

$7 \times 10^{-4}$ , respectively. Close to perihelion, however, the comet-facing side of the spacecraft will be almost completely covered by dust during a single dust collection passage.

#### 4.5 Radiation Environment

In the following we predict the radiation levels received in the vicinity of the comet nucleus due to the presence of dust. It is beyond the scope of the present work to introduce a detailed wavelength-dependent model. Instead, values will only be given for the total amount of scattered visible light and thermally emitted radiation. The crucial parameters for these estimates are the albedo, phase function and temperature of the dust particles. We adopt the phase function derived for comet 1P/Halley [41] as shown in Figure 3, a dust geometric albedo of 4% [34], and a temperature at perihelion of 285 K (see Figure 5).

A priori it is not clear that it is valid to assume that the temperature of a particle of a given size is independent of its position in the coma, because the

gas molecules impacting on the particle surface give rise to a heat exchange between the gas and the dust phase. This effect was taken into account in early models [80, 81], but was found to be of minor importance later [43, 82]. Neglecting the heat exchange, the temperature of a dust particle is given by the equilibrium between incident radiation and thermal emission of the particle. If the coma is optically thin, which is shown to be true for the dust coma of 67P/C–G below, the incident radiation is dominated by solar illumination. Hence it is justified to treat the particle temperature as independent of the position in the coma. Assuming furthermore that the physical properties of the particles on their way from the inner to the outer coma do not change significantly, the infrared spectrum of dust near the nucleus can be approximated by the spectrum observed from Earth.

The thermal emission spectrum of cometary dust particles can only approximately be represented by the spectrum of a blackbody, because particles emit efficiently only at wavelengths smaller than their size. Consequently, the smallest (or very porous) particles have temperatures much higher than a blackbody at the given heliocentric distance, and it is not physically consistent to set the dust temperature to a constant value independent of particle size. However, for the purpose of estimating the amount of radiation received by an observer, only the properties of the dust particles as an ensemble are of importance. The relative contribution to the total cross section of particles of a given size in most of the coma volume is the same as in the ensemble seen by an Earth-based observer. This was found with the present model which consistently models the dynamics of particles of different sizes. To calculate the intensity received inside the coma it is therefore valid to assign every particle independently of its size the ensemble properties as measured in Earth-based observations, which is henceforth done for the optical and thermal characteristics of the particles.

Compared with the results given in the previous subsections – which were strongly controlled by model parameters only very indirectly accessible to ground-based observations (e.g. particle size distribution, particle density) – the results presented here only depend on parameters readily measured from ground. For example the estimates of the scattered visual radiation are governed solely by the  $Af\rho$  value and the dust phase function. It may, at first glance, be surprising that the results are not influenced by the dust albedo. However, because in the present model the overall dust activity is adjusted in order to match an observed  $Af\rho$  value, the predictions of the scattered visual radiation inside the coma are merely a scaling of the Earth-based observations to a different geometry. To give an idea of the accuracy of the results obtained for the scattered radiation: The present model applied to comet 1P/Halley during the fly-by of Giotto reproduces the measurements of the Halley Optical Probe experiment [83, 84] by a factor of only 1.5. By contrast, the predictions of the optical thickness and of the thermal radiation by the dust depend on more parameters, introducing uncertainty: The estimated optical thickness is

influenced by the dust albedo and by the – poorly constrained – extinction efficiency, while the thermal radiation relies on the dust temperature.

Using an extinction efficiency of  $q_{\text{ext}} = 1$  we find for the optical thickness at perihelion at the subsolar point values of  $\tau = 0.013$  in the insolation driven model and  $\tau = 0.09$  in the jet-model. In the insolation driven model the optical thickness of the coma along the line of sight from a point at the surface to the Sun is fairly constant over the comet surface and the results can well be approximated by the simplified model in [85]. In the jet model the optical thickness decreases towards the terminator by a factor of 5.

Since the extinction efficiency  $q_{\text{ext}}$  is little constrained and can assume values in the range  $q_{\text{ext}} \approx 1 - 2$  we estimate that at perihelion the optical thickness at the comet surface is typically in the range  $\tau \approx 0.01 - 0.03$ . Within jets it can reach values up to  $\tau \approx 0.2$ . Since the optical thickness is proportional to  $Af\rho$ , the results can easily be scaled to scenarios with different levels of cometary activity.

The intensity received by an observer at 4 km (2 comet radii) from the nucleus centre over the subsolar point for different lines of sight is shown in Figure 11. For the insolation driven model, the observed visible intensity reaches maxima for lines of sight directed towards the Sun and the nucleus (phase angle  $180^\circ$  and  $0^\circ$ , respectively). These peaks are not found in the infrared intensity received in the insolation driven model, which shows that they are due to the forward and backward scattering peaks of the dust phase function (Figure 3). In the insolation driven model the intensities, both for visible and infrared radiation, reach maxima for the lines of sight that touch the nucleus tangentially (at about  $150^\circ$ ). In the jet-model these peaks are not present because most of the dust is concentrated to a narrow region over the subsolar point. This also explains the maxima of the infrared intensity in the jet-model for the lines of sight in the Sun- and the nucleus-direction that are not observed in the insolation driven model. Correspondingly, the maxima for the visible radiation on these lines of sight are more pronounced in the jet-model than in the insolation driven model.

The total intensity received by a surface depends on its orientation. To give an example, we consider a plane surface at 4 km over the subsolar point (see Figure 12) taking into account also the radiation from the nucleus. The intensities emitted or scattered by the nucleus dominate over those from the dust; and, since the nucleus is a dark object, the infrared radiation dominates the total intensity. Note that the nucleus temperature in the model is calculated as that of a pure icy surface. Thus the given results for the infrared radiation received from the nucleus are lower limits. If the major part of the comet surface is inactive, the surface temperature and consequently the infrared flux will be much higher.

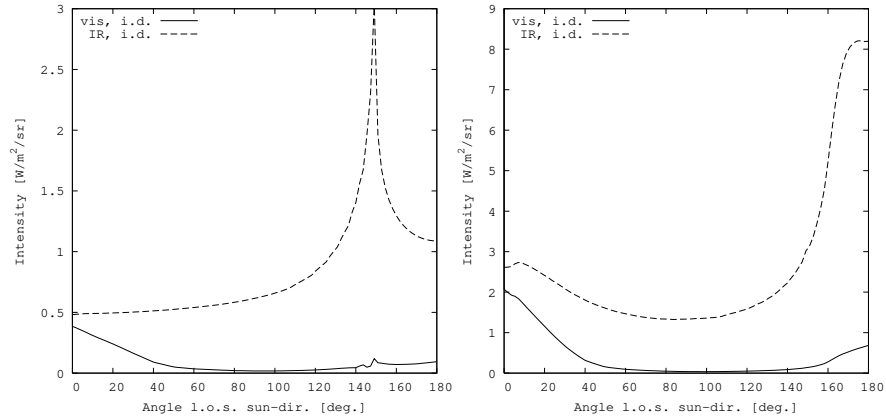


**Fig. 11** Scattered sunlight and thermal infrared radiation at perihelion received from a line of sight by an observer above the subsolar point at 4 km from the nucleus centre. Only the contribution by the dust is considered, in contrast to radiation from the nucleus or direct sunlight. The nominal size distribution  $\alpha = -3.7$  was used. Left: insolation driven model, right: jet model.

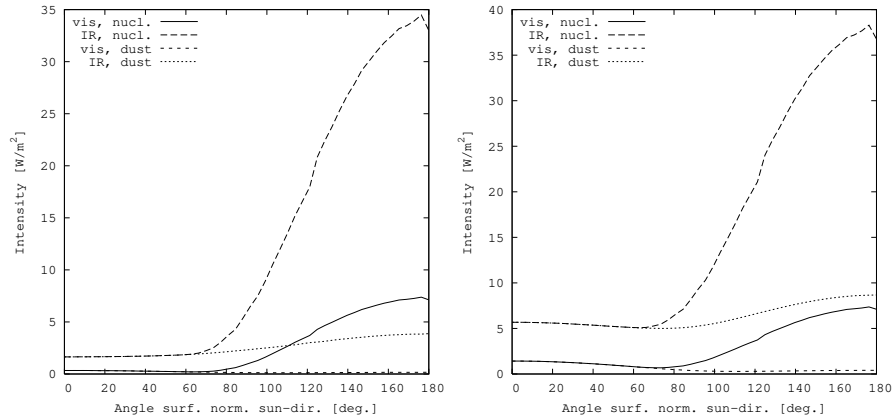


**Fig. 12** Radiation at perihelion from all directions on a surface above the subsolar point at 4 km from the nucleus centre. Both curves with and without the contribution from the nucleus are shown, but no direct sunlight is considered. The nominal size distribution  $\alpha = -3.7$  was used. Left: insolation driven model, right: jet model.

## 5 Summary and Conclusions

We have summarised the present knowledge on the dust emitted by Rosetta target comet 67P/Churyumov-Gerasimenko and discussed methods and results of modelling it. The observational data can be described as follows: The dust and gas production rates peaked about 30 days after perihelion passage during three past apparitions. The coma was characterised by az-

imuthal brightness variations probably resulting from active areas on the surface. Close to the comet orbit, a distinct line-shaped feature prevailed at least from shortly after perihelion 2002 until 2006, beyond aphelion. It is interpreted as a pronounced antitail due to the low inclination of the comet orbital plane towards the ecliptic. The colour temperatures in both the coma and the trail were higher than the blackbody equilibrium temperature at the concerned heliocentric distance.

We have reviewed different approaches to derive parameters of the cometary dust production by modelling images of the tail and/or trail, and the results obtained by their application to observations of 67P/C-G. We found that due to the large diversity of the derived parameter values it is at present not possible to formulate a consistent picture of the 67P/C-G dust activity and its time evolution. We identified the need to find a common model that satisfies all available observations.

Using the ESA Cometary Dust Environment Model we have predicted the terminal speeds of dust, the dust flux in the coma and along sample trajectories of the spacecraft, and the radiation flux in the coma. We listed results for three mass distributions and five heliocentric distances. We also considered different surface activity distributions, among which one implying a homogeneous surface of the nucleus and one assuming all dust to be emitted by a single active area. The former yielded estimates of quantities averaged over space and time, while the latter served to derive upper limits for local quantities.

**Acknowledgements** M. M. gratefully acknowledges funding by EDS Operations Services GmbH. We wish to thank R. Schulz et al. [19, 20] for making their data available to us.

## References

1. M.L. Finson, R.F. Probst, *ApJ* **154**, 327 (1968)
2. E. Grün, E.K. Jessberger, in *Physics and Chemistry of Comets*, ed. by W. Huebner (1990), pp. 113–176
3. H.U. Keller, W.A. Delamere, H.J. Reitsemma, W.F. Huebner, H.U. Schmidt, *A&A* **187**, 807 (1987)
4. N. Thomas, H.U. Keller, *A&A* **187**, 843 (1987)
5. L.A. Soderblom, D.C. Boice, D.T. Britt, R.H. Brown, B.J. Buratti, R.L. Kirk, M. Lee, R.M. Nelson, J. Oberst, B.R. Sandel, S.A. Stern, N. Thomas, R.V. Yelle, *Icarus* **167**, 4 (2004). DOI 10.1016/S0019-1035(03)00266-5
6. Z. Sekanina, D.E. Brownlee, T.E. Economou, A.J. Tuzzolino, S.F. Green, *Science* **304**, 1769 (2004). DOI 10.1126/science.1098388
7. M. Müller, E. Grün, ESA-RO-ESC-TA-5501 (1997)
8. M. Müller, E. Grün, ESA-RO-ESC-TA-5501 (1998)
9. M. Müller, PhD Thesis, Universität Heidelberg. (1999)
10. M. Landgraf, M. Müller, E. Grün, *Planet. Space Sci.* **47**, 1029 (1999)
11. H. Kimura, C. Liu, *Chin. Astron.* **1**, 235 (1977)

12. K. Richter, W. Curdt, H.U. Keller, *A&A* **250**, 548 (1991)
13. M. Müller, S.F. Green, N. McBride, in *ESA SP-495: Meteoroids 2001 Conference* (2001), pp. 47–54
14. H. Boehnhardt, *Earth Moon and Planets* **93**, 19 (2003). DOI 10.1023/B:MOON.0000034496.28985.ef
15. M.V. Sykes, L.A. Lebofsky, D.M. Hunten, F. Low, *Science* **232**, 1115 (1986)
16. M.V. Sykes, D.M. Hunten, F.J. Low, *Advances in Space Research* **6**, 67 (1986)
17. M.V. Sykes, R.G. Walker, *Icarus* **95**, 180 (1992)
18. D.G. Schleicher, *Icarus* **181**, 442 (2006). DOI 10.1016/j.icarus.2005.11.014
19. R. Schulz, J.A. Stüwe, H. Bönhardt, *A&A* **422**, L19 (2004)
20. R. Schulz, J.A. Stüwe, H. Bönhardt, in *ASSL Vol. 311: The New Rosetta Targets. Observations, Simulations and Instrument Performances*, ed. by L. Colanageli, E. Mazzotta Epifani, P. Palumbo (2004), pp. 15–24
21. M. Weiler, H. Rauer, J. Helbert, *A&A* **414**, 749 (2004)
22. M. Fulle, C. Barbieri, G. Cemonese, H. Rauer, M. Weiler, G. Milani, R. Ligustri, *A&A* **422**, 357 (2004)
23. F. Moreno, L.M. Lara, O. Muñoz, J.J. López-Moreno, A. Molina, *ApJ* **613**, 1263 (2004). DOI 10.1086/423268
24. J. Agarwal, H. Bönhardt, E. Grün, in *ESA SP-643: Dust in Planetary Systems*, ed. by H. Krüger, A. Graps (2007), pp. 51–54
25. J. Agarwal, *The Emission of Large Dust Particles from Comet 67P/Churyumov-Gerasimenko Constrained by Observation and Modelling of its Dust Trail*. Ph.D. thesis, Universität Heidelberg (2007)
26. M. Ishiguro, *Icarus* **193**, 96 (2008)
27. M.S. Kelley, W.T. Reach, D.J. Lien, *Icarus* **193**, 572 (2008). DOI 10.1016/j.icarus.2007.08.018
28. M.S. Hanner, R.H. Giese, K. Weiss, R. Zerull, *A&A* **104**, 42 (1981)
29. C.W. Allen, *Astrophysical quantities* (London: University of London, Athlone Press, —c1973, 3rd ed., 1973)
30. R.L. Millis, M.F. Ahearn, D.T. Thompson, *AJ* **87**, 1310 (1982). DOI 10.1086/113218
31. K.J. Meech, D.C. Jewitt, *A&A* **187**, 585 (1987)
32. D.G. Schleicher, R.L. Millis, P.V. Birch, *Icarus* **132**, 397 (1998). DOI 10.1006/icar.1997.5902
33. A.T. Tokunaga, W.F. Golisch, D.M. Griep, C.D. Kaminski, M.S. Hanner, *AJ* **92**, 1183 (1986). DOI 10.1086/114251
34. M.S. Hanner, E. Tedesco, A.T. Tokunaga, G.J. Veeder, D.F. Lester, F.C. Wittetborn, J.D. Bregman, J. Gradie, L. Lebofsky, *Icarus* **64**, 11 (1985)
35. M.S. Hanner, R.L. Newburn, *AJ* **97**, 254 (1989). DOI 10.1086/114977
36. R.D. Gehrz, E.P. Ney, *Icarus* **100**, 162 (1992). DOI 10.1016/0019-1035(92)90027-5
37. E.P. Ney, *Icarus* **23**, 551 (1974)
38. E.P. Ney, K.M. Merrill, *Science* **194**, 1051 (1976)
39. E.P. Ney, *Optical and infrared observations of bright comets in the range 0.5 micrometers to 20 micrometers*. In *Comets (L. Wilkening, ed.)* (Univ. of Arizona, Tucson, 1982), pp. 323–340
40. L. Kolokolova, M.S. Hanner, A.C. Levasseur-Regourd, B.Å.S. Gustafson, in *Comets II*, ed. by M.C. Festou, H.U. Keller, H.A. Weaver (2004), pp. 577–604
41. N. Divine, in *ESA SP-174: The Comet Halley. Dust and Gas Environment* (1981), pp. 47–53
42. J.A.M. McDonnell, P.L. Lamy, G.S. Pankiewicz, in *ASSL Vol. 167: IAU Colloq. 116: Comets in the post-Halley era*, ed. by R.L. Newburn, Jr., M. Neugebauer, J. Rahe (1991), pp. 1043–1073



43. N. Divine, H. Fechtig, T.I. Gombosi, M.S. Hanner, H.U. Keller, S.M. Larson, D.A. Mendis, R.L. Newburn, R. Reinhard, Z. Sekanina, D.K. Yeomans, *Space Science Reviews* **43**, 1 (1986)
44. M.F. A'Hearn, D.G. Schleicher, R.L. Millis, P.D. Feldman, D.T. Thompson, *AJ* **89**, 579 (1984)
45. A.D. Storrs, A.L. Cochran, E.S. Barker, *Icarus* **98**, 163 (1992)
46. D.J. Osip, D.G. Schleicher, R.L. Millis, *Icarus* **98**, 115 (1992)
47. M.F. A'Hearn, R.L. Millis, D.G. Schleicher, D.J. Osip, P.V. Birch, *Icarus* **118**, 223 (1995)
48. M.R. Kidger, *A&A* **408**, 767 (2003)
49. P.L. Lamy, I. Toth, H. Weaver, L. Jorda, M. Kaasalainen, *AAS/Division for Planetary Sciences Meeting* **35** (2003)
50. P. Feldman, M. A'Hearn, M. Festou, in *ASSL Vol. 311: The New Rosetta Targets. Observations, Simulations and Instrument Performances*, ed. by L. Colangeli, E. Mazzotta Epifani, P. Palumbo (2004), pp. 47–52
51. J.T.T. Mäkinen, in *ASSL Vol. 311: The New Rosetta Targets. Observations, Simulations and Instrument Performances*, ed. by L. Colangeli, E. Mazzotta Epifani, P. Palumbo (2004), pp. 61–68
52. J. Crovisier, P. Colom, E. Gérard, D. Bockelée-Morvan, G. Bourgois, *A&A* **393**, 1053 (2002)
53. C. Tubiana, M. Drahus, H. Boehnhardt, L. Barrera, J. Ortiz, G. Schwehm, R. Schulz, in *AAS/Division for Planetary Sciences Meeting Abstracts, AAS/Division for Planetary Sciences Meeting Abstracts*, vol. 39 (2007), *AAS/Division for Planetary Sciences Meeting Abstracts*, vol. 39, p. #43.03
54. A.N. Cox, *Allen's astrophysical quantities* (Allen's astrophysical quantities, 4th ed. Publisher: New York: AIP Press; Springer, 2000. Edited by Arthur N. Cox. ISBN: 0387987460, 2000)
55. J.A.M. McDonnell, G.C. Evans, S.T. Evans, W.M. Alexander, W.M. Burton, J.G. Firth, E. Bussoletti, R.J.L. Grard, M.S. Hanner, Z. Sekanina, *A&A* **187**, 719 (1987)
56. S.F. Green, J.A.M. McDonnell, N. McBride, M.T.S.H. Colwell, A.J. Tuzzolino, T.E. Economou, P. Tsou, B.C. Clark, D.E. Brownlee, *Journal of Geophysical Research (Planets)* **109**(E18), E12S04 (2004). DOI 10.1029/2004JE002318
57. M. Fulle, L. Colangeli, V. Mennella, A. Rotundi, E. Bussoletti, *A&A* **304**, 622 (1995)
58. N. Divine, R.L. Newburn, *A&A* **187**, 867 (1987)
59. J.A.M. McDonnell, N. McBride, R. Beard, E. Bussoletti, L. Colangeli, P. Eberhardt, J.G. Firth, R. Grard, S.F. Green, J.M. Greenberg, *Nature* **362**, 732 (1993). DOI 10.1038/362732a0
60. A.J. Tuzzolino, T.E. Economou, B.C. Clark, P. Tsou, D.E. Brownlee, S.F. Green, J.A.M. McDonnell, N. McBride, M.T.S.H. Colwell, *Science* **304**, 1776 (2004). DOI 10.1126/science.1098759
61. F. Hörz, R. Bastien, J. Borg, J.P. Bradley, J.C. Bridges, D.E. Brownlee, M.J. Burchell, M. Chi, M.J. Cintala, Z.R. Dai, Z. Djouadi, G. Dominguez, T.E. Economou, S.A.J. Fairey, C. Floss, I.A. Franchi, G.A. Graham, S.F. Green, P. Heck, P. Hoppe, J. Huth, H. Ishii, A.T. Kearsley, J. Kissel, J. Leitner, H. Leroux, K. Marhas, K. Messenger, C.S. Schwandt, T.H. See, C. Snead, F.J. Stadermann, T. Stephan, R. Stroud, N. Teslich, J.M. Trigo-Rodríguez, A.J. Tuzzolino, D. Troadec, P. Tsou, J. Warren, A. Westphal, P. Wozniakiewicz, I. Wright, E. Zinner, *Science* **314**, 1716 (2006). DOI 10.1126/science.1135705
62. J.A. Burns, P.L. Lamy, S. Soter, *Icarus* **40**, 1 (1979). DOI 10.1016/0019-1035(79)90050-2
63. G. Mie, *Ann. Physik* **25**, 377 (1908)
64. C.F. Bohren, D.R. Huffman, *Absorption and scattering of light by small particles* (New York: Wiley, 1983, 1983)

65. B.A.S. Gustafson, J.M. Greenberg, L. Kolokolova, Y. Xu, R. Stognienko, in *Interplanetary Dust*, ed. by E. Grün, B.A.S. Gustafson, S.F. Dermott, H. Fechtig (2001), pp. 509–558
66. J. Agarwal, M. Müller, E. Grün, *Space Science Reviews* **128**, 79 (2007). DOI 10.1007/s11214-006-9139-1
67. T. Bredikhin, *Mechanische Untersuchungen über Cometenformen in systematischer Darstellung* (Ed. R. Jaegermann, St. Petersburg, Voss' Sortiment (G. Hassel), Leipzig, 1903), pp. 83–97
68. M.L. Finson, R.F. Probstein, *ApJ* **154**, 353 (1968)
69. J. Fertig, G.H. Schwehm, *Advances in Space Research* **4**, 213 (1984). DOI 10.1016/0273-1177(84)90030-9
70. M. Fulle, G. Sedmak, *Icarus* **74**, 383 (1988). DOI 10.1016/0019-1035(88)90110-8
71. M. Fulle, *A&A* **217**, 283 (1989)
72. D. Bockelée-Morvan, R. Moreno, N. Biver, J. Crovisier, J.F. Crifo, M. Fulle, M. Grewing, in *ASSL Vol. 311: The New Rosetta Targets. Observations, Simulations and Instrument Performances*, ed. by L. Colangeli, E. Mazzotta Epifani, P. Palumbo (2004), pp. 25–36
73. J. Agarwal, M. Müller, E. Grün, in *The New Rosetta Targets. Observations, Simulations and Instrument Performances, Astrophysics and Space Science Library*, vol. 311, ed. by L. Colangeli, E. Mazzotta Epifani, P. Palumbo (2004), *Astrophysics and Space Science Library*, vol. 311, pp. 143–152
74. B.E.A. Mueller, in *Asteroids, Comets, Meteors 1991*, ed. by A.W. Harris, E. Bowell (1992), pp. 425–428
75. S.C. Lowry, A. Fitzsimmons, S. Collander-Brown, *A&A* **397**, 329 (2003). DOI 10.1051/0004-6361:20021486
76. G. Tancredi, J.A. Fernández, H. Rickman, J. Licandro, *A&A Suppl. Ser.* **146**, 73 (2000)
77. G. Tancredi, J.A. Fernández, H. Rickman, J. Licandro, *Icarus* **182**, 527 (2006). DOI 10.1016/j.icarus.2006.01.007
78. P.L. Lamy, I. Toth, B.J.R. Davidsson, O. Groussin, P. Gutiérrez, L. Jorda, M. Kaasalainen, S.C. Lowry, *Space Science Reviews* **128**, 23 (2007). DOI 10.1007/s11214-007-9146-x
79. D. Koschny, V. Dhiri, K. Wirth, J. Zender, R. Solaz, R. Hoofs, R. Laureijs, T.M. Ho, B. Davidsson, G. Schwehm, *Space Science Reviews* **128**, 167 (2007). DOI 10.1007/s11214-006-9129-3
80. R.F. Probstein, in *Problems of Hydrodynamics and Continuum Mechanics, SIAM*, ed. by M.A. Lavrentev (1968), pp. 568–583
81. Y. Kitamura, *Icarus* **66**, 241 (1986)
82. J. Knollenberg, PhD Thesis, Georg-August-Universität, Göttingen (1994)
83. A.C. Levasseur-Regourd, J.L. Bertaux, R. Dumont, M. Festou, R.H. Giese, F. Giovane, P. Lamy, J.M. Le Blanc, A. Llebaria, J.L. Weinberg, *Nature* **321**, 341 (1986)
84. M. Fulle, A.C. Levasseur-Regourd, N. McBride, E. Hadamcik, *AJ* **119**, 1968 (2000). DOI 10.1086/301285
85. M. Müller, S.F. Green, N. McBride, *Earth Moon and Planets* **90**, 99 (2002)